AGU PUBLICATIONS

JGR

Journal of Geophysical Research: Solid Earth

RESEARCH ARTICLE
10.1002/2017JB014513

Key Points:
- HR-EBSD map distributions of GND density and elastic stress/strain in experimentally deformed single crystals of olivine
- Short-range dislocation interactions impeded glide, resulting in locally elevated GND densities, commonly along slip bands
- GNDs generate heterogeneous internal stress fields which may influence microstructural organization over micron length scales

Correspondence to:
D. Wallis,
david.wallis@earth.ox.ac.uk

Citation:
Wallis, D., Hansen, L. N., Britton, T. B., & Wilkinson, A. J. (2017). Dislocation interactions in olivine revealed by HR-EBSD. *Journal of Geophysical Research: Solid Earth*, *122*, 7659–7678. https://doi.org/10.1002/2017JB014513

Received 1 JUN 2017
Accepted 31 AUG 2017
Accepted article online 4 SEP 2017
Published online 21 OCT 2017

Dislocation Interactions in Olivine Revealed by HR-EBSD

David Wallis[1], Lars N. Hansen[1], T. Ben Britton[2], and Angus J. Wilkinson[3]

[1]Department of Earth Sciences, University of Oxford, Oxford, UK, [2]Department of Materials, Imperial College London, London, UK, [3]Department of Materials, University of Oxford, Oxford, UK

Abstract Interactions between dislocations potentially provide a control on strain rates produced by dislocation motion during creep of rocks at high temperatures. However, it has been difficult to establish the dominant types of interactions and their influence on the rheological properties of creeping rocks due to a lack of suitable observational techniques. We apply high-angular resolution electron backscatter diffraction to map geometrically necessary dislocation (GND) density, elastic strain, and residual stress in experimentally deformed single crystals of olivine. Short-range interactions are revealed by cross correlation of GND density maps. Spatial correlations between dislocation types indicate that noncollinear interactions may impede motion of proximal dislocations at temperatures of 1000°C and 1200°C. Long-range interactions are revealed by autocorrelation of GND density maps. These analyses reveal periodic variations in GND density and sign, with characteristic length scales on the order of 1–10 μm. These structures are spatially associated with variations in elastic strain and residual stress on the order of 10^{-3} and 100 MPa, respectively. Therefore, short-range interactions generate local accumulations of dislocations, leading to heterogeneous internal stress fields that influence dislocation motion over longer length scales. The impacts of these short- and/or long-range interactions on dislocation velocities may therefore influence the strain rate of the bulk material and are an important consideration for future models of dislocation-mediated deformation mechanisms in olivine. Establishing the types and impacts of dislocation interactions that occur across a range of laboratory and natural deformation conditions will help to establish the reliability of extrapolating laboratory-derived flow laws to real Earth conditions.

1. Introduction

The viscosities of olivine-rich peridotites in the upper mantle exert a control on the rates and styles of many tectonic processes (Turcotte & Oxburgh, 1972). Flow laws derived from laboratory experiments predict that the viscosities of such rocks are in turn commonly controlled by rates of dislocation motion during deformation of olivine by dislocation creep or dislocation-accommodated grain boundary sliding (Hansen et al., 2012; Hirth & Kohlstedt, 2003; Kohlstedt & Hansen, 2015). However, such predictions require extrapolations across several orders of magnitude in strain rate and to a lesser extent in stress (Hirth & Kohlstedt, 2003; Karato & Wu, 1993; Paterson, 1976). Confidence in predicted flow properties can be gained if the rate-limiting microphysical processes can be identified and demonstrated to be the same in both the laboratory and natural settings (Hirth & Kohlstedt, 2015; Paterson, 1976). However, it remains unresolved whether strain rate during power law creep of olivine is limited by the rate at which dislocations overcome lattice resistance during glide (Cooper et al., 2016) or the rate at which they climb to overcome obstacles (Hirth & Kohlstedt, 2015; Weertman, 1970). Distinguishing between these possibilities would be aided by improved characterization of the microstructural factors that influence the stress required for glide, the resistance they impose, and the means by which they are overcome.

Within grain interiors, interactions between dislocations potentially provide an impediment to dislocation glide, requiring either increased stress or recovery by climb/cross-slip for glide to continue. Dislocation morphologies in olivine deformed at 800–900°C, and large differential stresses (up to ~1 GPa) suggest that interactions between dislocations with the same Burgers vector, primarily [001], impede dislocation glide (Mussi et al., 2015). This finding is supported by simple elastic analysis and more complex 3-D simulations of dislocation dynamics (Durinck et al., 2007). In contrast, experiments conducted at 1550–1600°C on single crystals of olivine revealed no evidence that interactions between different dislocation types modified either the microstructure or mechanical behavior (Durham et al., 1985). These previous studies suggest that the significance (and possibly the nature) of dislocation interactions in olivine may vary with temperature. This implication motivates investigation of dislocation interactions in

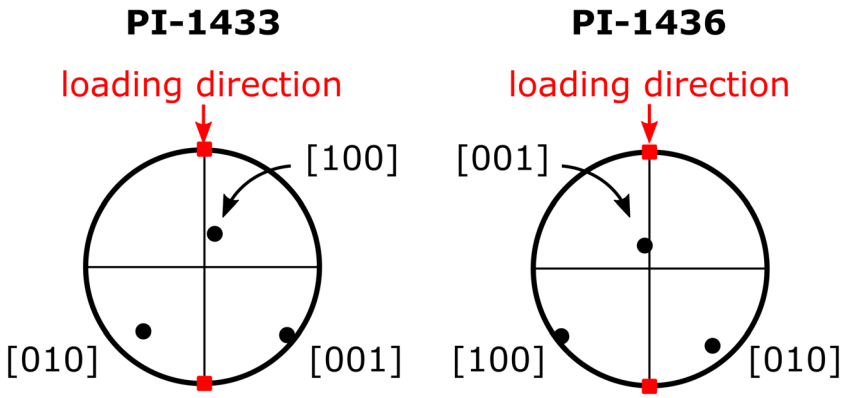

Figure 1. Lower hemisphere stereographic projections of loading directions of samples PI-1433 and PI-1436 relative to the crystal orientations in the reference frame of the EBSD maps.

olivine deformed at temperatures intermediate to those above and which typify the shallow upper mantle and many deformation experiments.

We employ high-angular resolution electron backscatter diffraction (HR-EBSD), developed in the materials sciences (Britton & Wilkinson, 2011, 2012a, 2012b; Wilkinson et al., 2006) and recently adapted to analyze olivine (Wallis et al., 2016). HR-EBSD is used to map lattice rotations and elastic strain variations in single crystals of olivine deformed at 1000°C and 1200°C. These data are used to estimate densities of geometrically necessary dislocations (GNDs) and heterogeneities in residual stress to investigate dislocation interactions. The use of single crystals allows analysis of microstructures and stress fields that developed without the complicating effects of compatibility constraints imposed by neighboring grains (Bai & Kohlstedt, 1992; Demouchy et al., 2013; Girard et al., 2013; Kohlstedt & Goetze, 1974; Mackwell et al., 1985; Mussi et al., 2015). This approach isolates the effects that arise solely from interactions among dislocations within a single grain. We analyze the GND density distributions in detail to (1) test whether they preserve evidence for particular dislocation interactions, (2) interpret controls on the development of intragranular substructure and stress fields, and (3) infer the impacts of these processes on rheological properties of olivine during high-temperature creep.

2. Methods

2.1. Deformation Experiments

We analyze two samples consisting of single crystals of San Carlos olivine (approximately Fo_{90}). The samples were deformed in experiments described in detail by Schneider (2008) and similar to those of Demouchy et al. (2009). Here we summarize the most relevant aspects of the experiments. Samples were oriented with Laue X-ray back-reflection diffraction. For sample PI-1433, the loading direction approximately bisected the [010] and [001] directions (the $[011]_c$ direction). For PI-1436, the loading direction approximately bisected the [100] and [010] directions (the $[110]_c$ direction) (Figure 1). Samples were cut as square parallelepipeds approximately 4.4 × 4.4 mm in cross section and 8.0 mm in length. Samples were coated in powdered orthopyroxene to buffer silica activity, and then jacketed in nickel sleeves to maintain oxygen fugacity at the Ni/NiO buffer. Samples were deformed in a gas-medium apparatus (Paterson, 1990) at the University of Minnesota at a confining pressure of 300 ± 5 MPa. Experiments consisted of load-steps, in which the axial load was progressively increased. The $[011]_c$ sample was shortened to 7.25% longitudinal strain at 1000°C. The stress during the final load step was 388 MPa. The $[110]_c$ sample was shortened to 14.67% longitudinal strain at 1200°C. The stress during the final load step was 218 MPa. Samples were cooled to 400°C within 15 min immediately after unloading. The $[011]_c$ and $[110]_c$ loading directions correspond to the most viscous and least viscous orientations, respectively, observed in previous high-temperature creep experiments on single crystals of olivine (Bai et al., 1991; Durham & Goetze, 1977).

2.2. Sample Preparation and Data Acquisition

Samples were cut in sections containing the loading direction and approximately normal to a low-index direction (e.g., [100] for the $[011]_c$ sample; Figure 1). Specimen surfaces were polished with progressively

finer diamond suspensions with grit sizes from 15 μm down to 0.25 μm and finished by polishing with 0.03 μm colloidal silica. EBSD maps of both samples were collected using an FEI Quanta 650 FEG E-SEM equipped with an Oxford Instruments Nordlys-Nano EBSD camera and AZtec 2.1 acquisition software. Data were acquired in low-vacuum mode with 50 Pa chamber pressure to minimize charging while removing the need for coating. During data acquisition, diffraction patterns were stored for subsequent HR-EBSD post-processing. The map of the $[011]_c$ sample consists of 212 × 223 points at a step size of 1.25 μm and was collected with 2 × 2 binning of pixels in the diffraction patterns, giving 640 × 480 pixels in each pattern (Wallis et al., 2016). The map of the $[110]_c$ sample consists of 450 × 320 points at a step size of 1.0 μm and was collected without binning of pixels in the diffraction pattern, giving 1344 × 1024 pixels in each pattern. After acquisition of EBSD data, dislocations in both samples were decorated using the oxidation technique of Kohlstedt et al. (1976). The decorated dislocations were imaged using backscattered electrons at 5 kV accelerating voltage and 5 mm working distance.

2.3. HR-EBSD Analysis

Stored diffraction patterns were reanalyzed using the HR-EBSD approach of Wilkinson et al. (2006) and Britton and Wilkinson (2011, 2012a). A reference pattern with high band contrast was chosen from each map. One hundred regions of interest (ROIs) were selected from each diffraction pattern and cross correlated with the corresponding ROIs in the reference pattern to determine the relative shift of each ROI. A displacement gradient tensor was fitted to the shifts in each pattern, allowing calculation of the lattice rotations and elastic strains relative to the reference pattern, both with a sensitivity of approximately 10^{-4} (Wilkinson et al., 2006). Residual stress variations were calculated from the elastic strain variations using the elastic moduli of olivine at 1 atm and 273 K (Abramson et al., 1997). In this analysis, the stress component normal to the sectioned specimen surface is assumed to be relaxed to zero. Strains are calculated in the reference frame of the microscope stage, but we present components of the stress tensor in the crystal reference frame to aid interpretation of their impact on dislocation processes.

The measured values of elastic strain, and hence residual stress, are relative to the strain state of the reference pattern. For samples in this study, the majority of the sample material appears to be under some residual elastic strain, and therefore, it is not possible to pick unstrained reference patterns. As a result, the measured values are relative to the unknown strain state of the reference patterns. Nonetheless, the results document the magnitude of *heterogeneity* in both elastic strain and residual stress. We follow the approach of Jiang et al. (2013a) and Mikami et al. (2015) by subtracting the mean of each component of the stress heterogeneities from the measured stress state at each point (i.e., normalizing the mean of each stress component to zero). This recasts the results as stress heterogeneities relative to the mean stress state in each map. Assuming that any externally applied deviatoric stresses (i.e., exerted by the jackets) on the crystals during mapping were negligible and that the maps cover sufficient area that the mean stress state of the mapped region approximates that of the whole crystal (N.B. the caveat of stresses normal to the specimen surface being relaxed), then the normalized stress heterogeneities approximate the absolute stress states.

Densities of geometrically necessary dislocations (GNDs) were estimated from the lattice rotations through analysis of the Nye tensor (Nye, 1953). The Nye tensor is a function of gradients in both lattice rotations and elastic strains (Wilkinson & Randman, 2010), but the former are an order of magnitude larger than the latter in this application. Thus, we neglect elastic strain gradients in our GND analysis. The GND analysis used here follows the pseudoinversion method of Wallis et al. (2016), whereby six common types of dislocation (those presented in Figures 5 and 6) are specified a priori, and the densities of each are calculated to fit the measured gradients in lattice orientation. As six components of the lattice curvature can be measured from 2-D EBSD maps, consideration of no more than six types of dislocations results in a single, best fit solution for the densities of each type (Wallis et al., 2016). This simple approach contrasts with those employed in previous work on metals where the multitude of slip systems requires additional assumptions or constraints to select one of many possible combinations of dislocation types and densities to fit the measured lattice orientation gradients (Jiang et al., 2015; Wilkinson & Randman, 2010). The apparent density of GNDs depends on the mapping step size and, to a lesser extent, on the binning of pixels in diffraction patterns (Jiang et al., 2013b; Ruggles et al., 2016; Wallis et al., 2016). Wallis et al. (2016) presented a detailed assessment of these effects for the same map of PI-1433 as used in this study. The differences in step size and binning between the two maps reported here have negligible impacts on the GND density results. In addition, unlike the

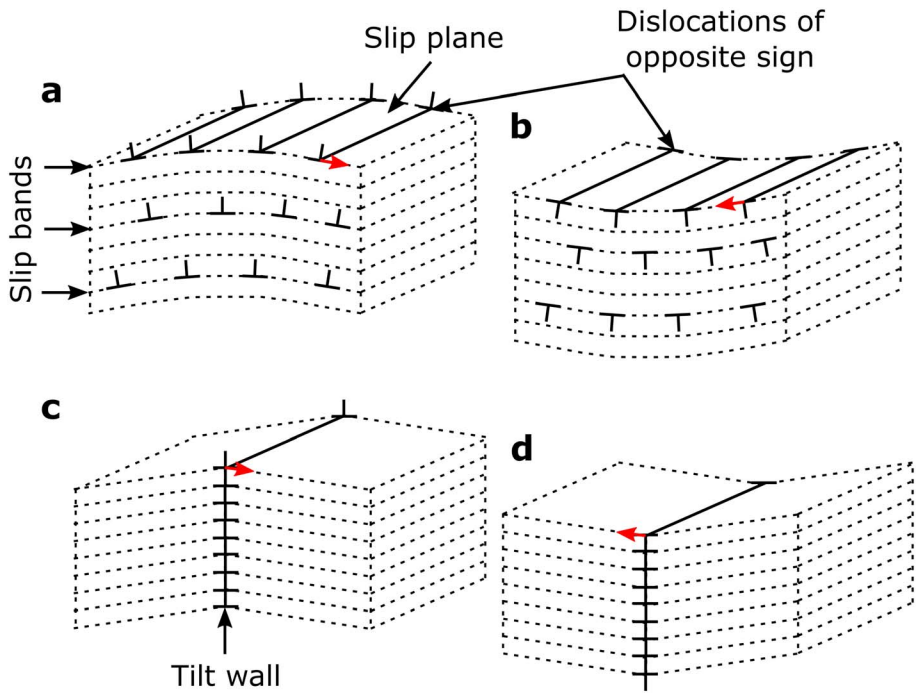

Figure 2. Schematic illustration of edge dislocations of opposite sign arranged into (a and b) slip bands and (c and d) tilt walls. The red arrows indicate the direction of Burgers vector.

estimates of elastic strains, estimates of GND densities do not depend on the choice of reference pattern. Moreover, our analysis focuses on the relative densities of different types of dislocation, which can be reliably estimated from the map data. We denote both positive and negative densities of each type of GND to discriminate between dislocations of the same general type but with opposite Burgers vectors (for the same line direction). Opposite Burgers vectors lead to opposing senses of lattice curvature, as illustrated schematically in Figure 2 for slip bands and tilt walls.

We used cross correlation and autocorrelation of the GND density maps to characterize the GND distributions in more detail. We used normalized cross correlation between maps of the absolute density of each dislocation type to assess the degree to which different types of dislocation are spatially coincident. The resulting correlation coefficients provide quantitative measurements of the spatial coincidence of dislocation types. 2-D autocorrelation functions, computed for maps of individual dislocation types, characterize the directionality and periodicity of the GND distributions. Positive values in the autocorrelation function indicate correlation, whereas negative values indicate anticorrelation. All autocorrelation functions are normalized to a maximum peak height of one. We present 1-D representations of the autocorrelation functions by radially averaging over each quadrant of the 2-D functions. Periodicity within particular quadrants records the characteristic length scales of the GND distributions, whereas differences between quadrants reflect directionality in the GND distributions.

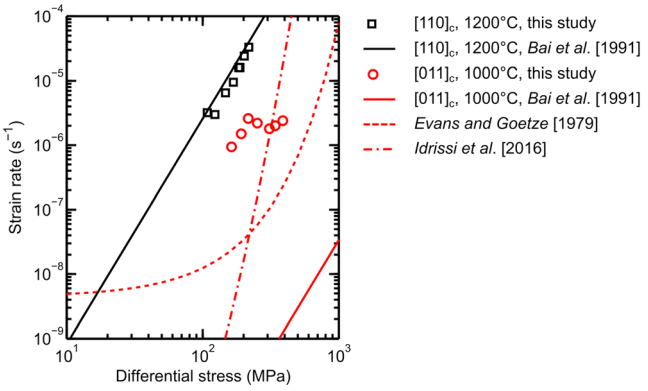

Figure 3. Mechanical data from load stepping tests on samples deformed in the $[011]_c$ and $[110]_c$ orientations at 1000°C and 1200°C, respectively. The lines indicate strain rates predicted by previously published flow laws for dislocation creep (Bai et al., 1991) and low-temperature plasticity (Evans & Goezte, 1979; Idrissi et al., 2016).

3. Results

3.1. Mechanical Data

Figure 3 presents strain rates measured during load steps in the two experiments. The $[011]_c$ sample deformed at strain rates in the range 9.4×10^{-7}–2.4×10^{-6} s^{-1} under stresses of 163–388 MPa. The data do not lie on a well-defined line in Figure 3, preventing determination of

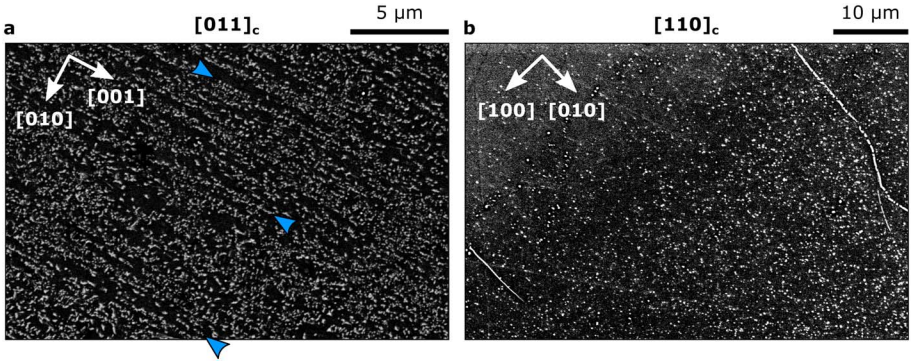

Figure 4. Decorated dislocations in the $[011]_c$ and $[110]_c$ samples. The traces of crystal axes are annotated, and the loading direction was top-bottom. (a) The blue arrows mark examples of clusters of dislocations arranged in bands parallel to the trace of [001] in the $[011]_c$ sample. These are consistent with the presence of slip bands of (010)[001] edge dislocations. (b) The $[110]_c$ sample contains gradients in dislocation density (top left to bottom right) over distances of tens of micrometers. The white lines in the $[110]_c$ sample are decorated microcracks.

a stress exponent for this sample. The $[110]_c$ sample deformed at strain rates in the range 3.2×10^{-6}–3.3×10^{-5} s^{-1} under stresses of 108–218 MPa. In Figure 3 the results from the $[110]_c$ sample define a straight line with a gradient that indicates a stress exponent of 3.5.

3.2. Decorated Dislocations

Backscattered electron images of dislocations decorated using the oxidation method of Kohlstedt et al. (1976) reveal different distributions of dislocations in the two samples (Figure 4). The density of dislocations evident in the image of the $[011]_c$ sample is 1.5×10^{13} m^{-2} (Figure 4a). This sample contains dislocations arranged in linear structures aligned with the [001] axis (Figure 4a). These sets of aligned dislocations are consistent with the presence of slip bands (Figures 2a and 2b) of (010)[001] edge dislocations, which are expected to be activated in the $[011]_c$ loading orientation (Figure 1). This hypothesis is explored in detail below. Typically, dislocations are unevenly distributed along these bands, forming clusters a few micrometers in length (examples marked by blue arrows in Figure 4a). In contrast, the $[110]_c$ sample lacks these linear arrays of decorated dislocations (Figure 4b). Instead, dislocations in the $[110]_c$ sample appear randomly distributed but exhibit gradients in dislocation density (top left to bottom right in Figure 4b) over distances of tens of micrometers. The dislocation density in the top left of Figure 4b is 2.1×10^{11} m^{-2}, whereas in the bottom right of the image the dislocation density is 1.6×10^{12} m^{-2}.

3.3. Lattice Rotations and Geometrically Necessary Dislocations

Sets of intragranular structures are evident in the maps of lattice rotations in both samples (Figures 5 and 6). Components of the rotation matrix describing lattice rotations relative to the reference points reach magnitudes up to approximately 10^{-2} radians (approximately 0.6°) within each map area (Figures 5 and 6). However, much of the fine structure visible in the maps results from rotations on the order of 10^{-3} radians or ~0.05° (Figures 5 and 6). The $[011]_c$ sample contains two sets of structures that are evident in the maps of rotations (black and blue arrows in Figure 5). One prominent set of structures trends top right to bottom left and is visible in maps of each off-diagonal term of the rotation matrix (black arrows in Figure 5, hereafter termed Set 1). A second set of structures consisting of much lower magnitude rotations trends top left to bottom right and is most evident in the map of the ω_{12} component of the rotation matrix (blue arrows in Figure 5, Set 2). The $[110]_c$ sample also contains two sets of structures (grey and yellow arrows in Figure 6, Sets 3 and 4, respectively) with similar trends to those in the $[011]_c$ sample (Figure 5). Set 3 consists of broad bands, up to approximately 100 μm in width, with relative rotations on the order of 10^{-2} radians. Set 4 is evident in the map of the ω_{12} component of the rotation matrix and consists of short segments oriented top left to bottom right but arranged in linear arrays along the margins of the bands in Set 3. During acquisition of the EBSD data, secondary-electron images revealed that structures of Set 4 are related to arrays of short microcracks. Therefore, the apparent lattice rotations and GND densities associated

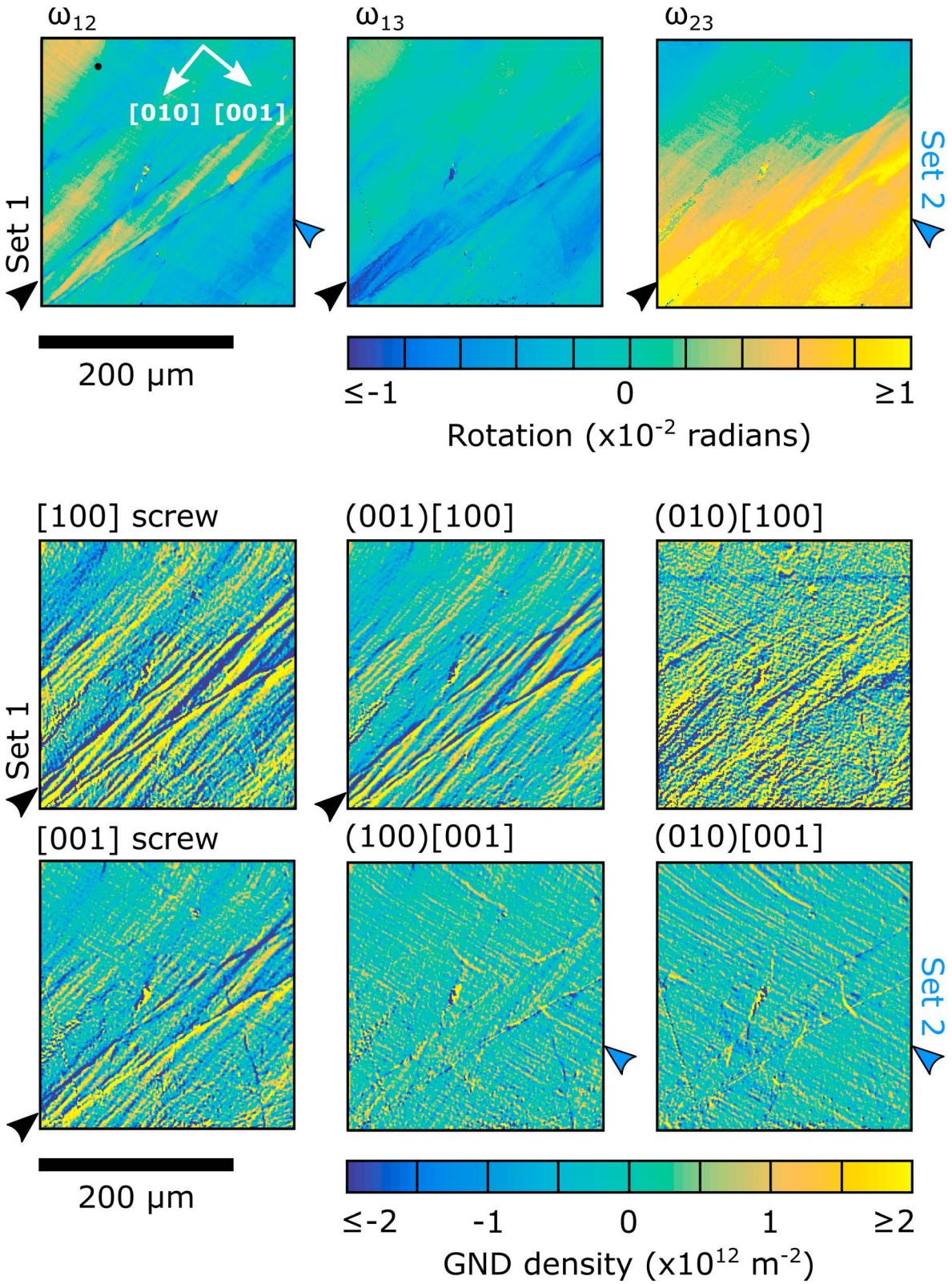

Figure 5. Lattice rotations and densities of geometrically necessary dislocations (GNDs) in the $[011]_c$ sample deformed at 1000°C and 388 MPa. Rotations are represented by one map for each off-diagonal component of the antisymmetric rotation tensor (ω_{ij}) describing the crystal orientation at each pixel relative to that of the reference point (black point in the map of ω_{12}). The black and blue arrows indicate structures of Set 1 (mixed character) and Set 2 (including bands of (010)[001] edge dislocations in slip band orientations). Projected crystal axes are marked in white.

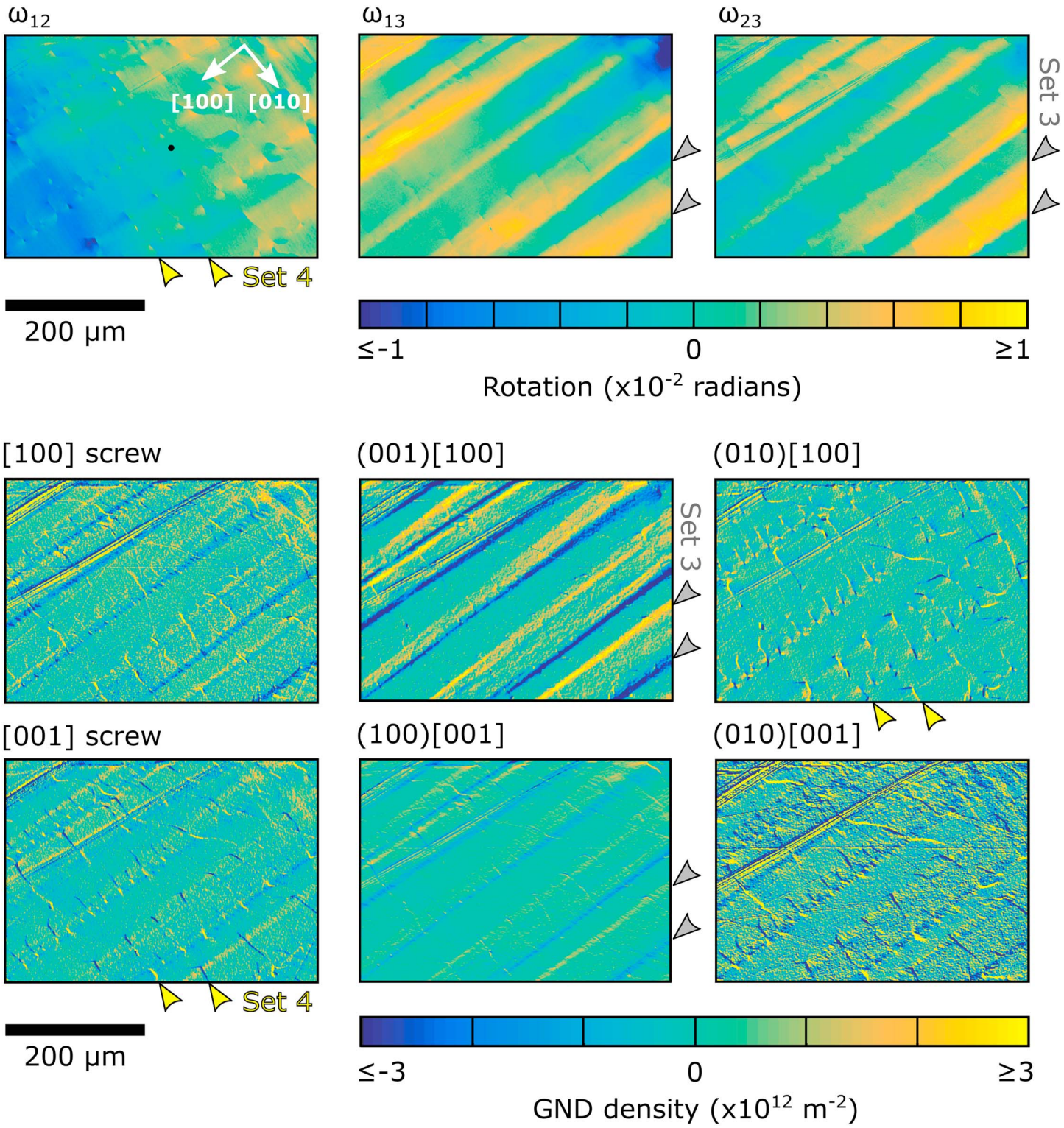

Figure 6. Lattice rotations and densities of geometrically necessary dislocations (GNDs) in the $[110]_c$ sample deformed at 1200°C and 218 MPa. Rotations are represented by one map for each off-diagonal component of the antisymmetric rotation tensor (ωij) describing the crystal orientation at each pixel relative to that of the reference point (black point in the map of ω12). The grey and yellow arrows indicate structures of Set 3 (predominantly bands of (001)[100] edge dislocations in slip band orientations) and Set 4 (apparent GND density associated with microcracks). Projected crystal axes are marked in white.

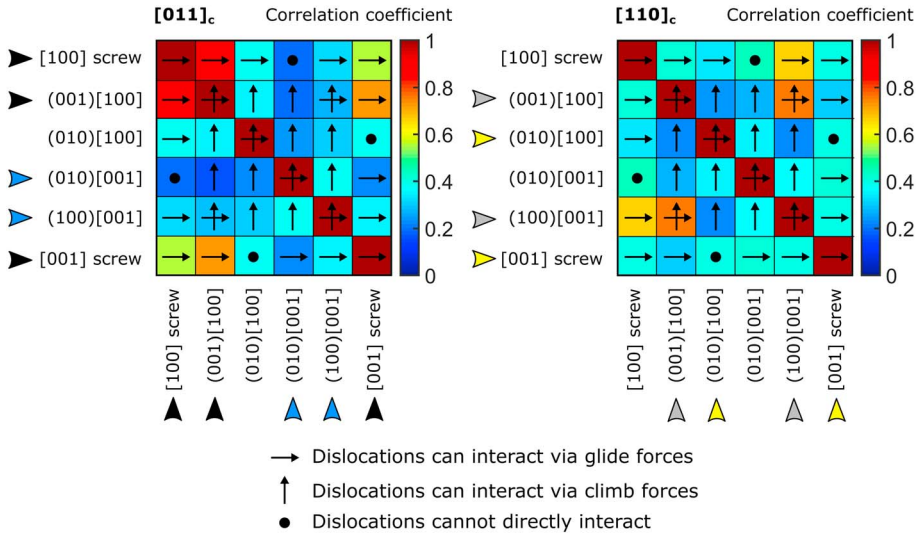

Figure 7. Look-up tables of the correlation coefficients between maps of the absolute densities of each pair of dislocation types in the $[011]_c$ and $[110]_c$ samples. Values close to one indicate strong correlation between dislocation types, whereas values close to zero indicate poor correlation. Symbols denote the possibilities for interactions between each pair of dislocation types based on the Peach-Koehler equation (Peach & Koehler, 1950) assuming straight dislocations of pure edge or screw character. The arrows indicate the dislocation types involved in sets of structures marked in Figures 5 and 6.

with Set 4 likely result from small rotation gradients associated with the microcracks and should not be interpreted in terms of dislocation processes.

Maps of each dislocation type exhibit sets of structures comparable to one or more of those sets evident in the maps of lattice rotations (Figures 5 and 6). Densities of GNDs within these structures are on the order of 10^{12} m^{-2} in both samples. Wallis et al. (2016) provided preliminary characterization of the dislocation structures in the $[011]_c$ sample, and here we characterize them in more detail. Set 1 consists primarily of (001)[100] edge dislocations and screw dislocations with both [100] and [001] Burgers vectors. Set 2 consists primarily of (100)[001] and (010)[001] edge dislocations with lower densities of GNDs and closer spacing of the bands compared to Set 1. Edge dislocations of (010)[100] are present in similar densities to the other dislocation types but are distributed less coherently across both sets of structures (Figure 5). In many places it is evident that the sets of structures contain adjacent, and sometimes regularly alternating, bands of dislocations of the same type but opposite sign (Figure 5).

The $[110]_c$ sample also contains structures with alternating bands of dislocations of the same type but opposite sign (Figure 6). Set 3 consists primarily of (001)[100] edge dislocations, with more minor contributions from each of the other dislocation types, except (010)[100] edge dislocations. These bands are often separated by regions of much lower GND density (Figure 6). The microcracks of Set 4 appear in the GND density maps as short segments of *apparent* high GND density, probably due to slight rotations across the crack traces.

The spatial coincidence of each pair of dislocation types in a particular sample is evaluated in Figure 7 using cross correlation of the GND density maps in Figures 5 and 6 and based on the absolute densities of each dislocation type. The $[011]_c$ sample exhibits strong correlation between (001)[100] edge dislocations and [100] screw dislocations, which have a correlation coefficient of 0.88 (Figure 7). In both samples, notably elevated correlation coefficients also occur between dislocation types with nonparallel Burgers vectors (Figure 7). In the $[011]_c$ sample these correlations are between [001] screw dislocations and both (001)[100] edge dislocations (0.69) and [100] screw dislocations (0.55) (Figure 7). In the $[110]_c$ sample these correlations are between (100)[001] edge dislocations and both (001)[100] edge dislocations (0.75) and [100] screw dislocations (0.66) (Figure 7).

Additional details of the structures evident in each map of GND density are revealed by their autocorrelation functions in Figure 8. Several characteristics of the autocorrelation functions are similar among different dislocation types. Except for (010)[100] edge dislocations in the $[110]_c$ sample, autocorrelation functions

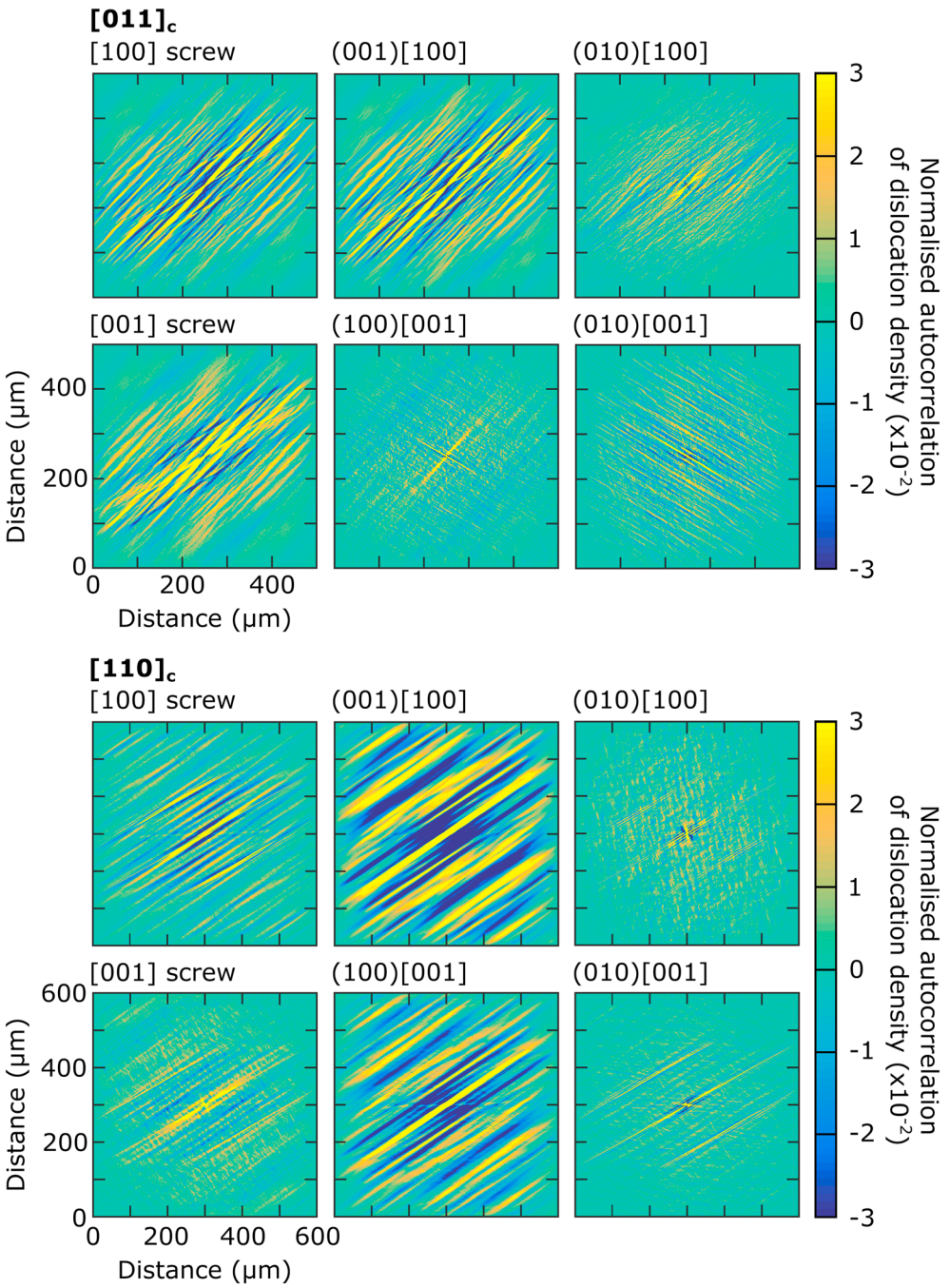

Figure 8. Autocorrelation functions of the GND density maps in Figures 5 and 6 for each dislocation type in the $[011]_c$ and $[110]_c$ samples, respectively. Each autocorrelation function is normalized by its maximum peak height.

for each dislocation type in both samples exhibit directionality and periodicity. In particular, the structure in the autocorrelation functions follows trends that reflect those of the underlying sets of GND density structures. The periodic structure of the autocorrelation functions contains bands of correlation (positive values) and anticorrelation (negative values), resulting from GNDs of either the same or opposite sign, respectively. The amplitudes and wavelengths of this periodicity vary between dislocation types.

Figure 9 presents 1-D radial averages of 2-D autocorrelation functions, including averages over all quadrants and over opposite quadrants. Several of these 1-D autocorrelation functions derived from averaging all quadrants reveal consistently positive correlation extending over length scales of a few micrometers to tens of

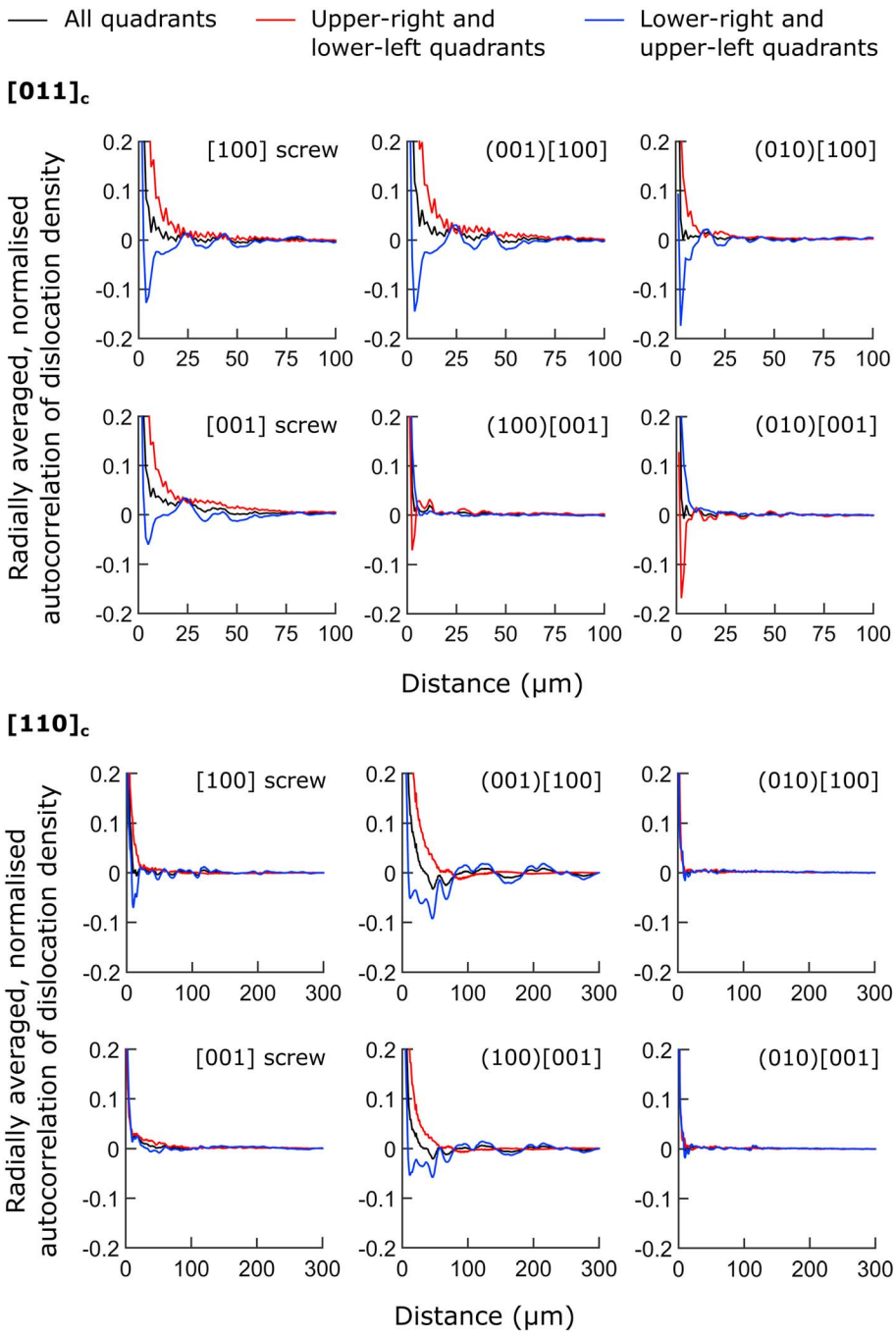

Figure 9. Radial averages of 2-D autocorrelation functions for each dislocation type. Positive values indicate correlation, negative values indicate anticorrelation, and values of zero indicate lack of correlation. Differences between averages for different quadrants of the autocorrelation function indicate directionality in the spatial distribution of dislocations.

micrometers. In particular, (001)[100] edge dislocations and both [100] and [001] screw dislocations in the $[011]_c$ sample exhibit correlation over approximately 15 μm. Similarly, (001)[100] and (100)[001] edge dislocations in the $[110]_c$ sample exhibit correlation over approximately 35 μm.

Comparisons between radial averages of specific quadrants of the autocorrelation functions characterize the directionality and periodicity evident in the maps of several dislocation types in both samples. In the $[011]_c$ sample, the bottom right and top left quadrants of the autocorrelation functions for (001)[100] and (010)[100] edge dislocations, as well as both [100] and [001] screw dislocations, exhibit periodic correlation and

anticorrelation with wavelengths of approximately 20 μm. In contrast, the top right and bottom left quadrants of the autocorrelation functions for these dislocation types exhibit correlation over distances greater than 20 μm.

The autocorrelation functions for (100)[001] and (010)[001] edge dislocations in the $[011]_c$ sample exhibit similar general characteristics but in the opposite quadrants. The top right and bottom left quadrants exhibit strong anticorrelation over distances of approximately 5 μm. Across longer length scales these quadrants reveal low-magnitude alternating correlation-anticorrelation with wavelengths of approximately 10 μm. The bottom right and top left quadrants of the autocorrelation functions for these dislocation types demonstrate correlation over 6–8 μm.

For the $[011]_c$ sample the strongest signals are present in the autocorrelation functions for (001)[100] and (100)[001] edge dislocations. These dislocation types exhibit correlation over distances of several tens of micrometers in the radial averages of the top right and bottom left quadrants and the full autocorrelation functions. However, the radial averages of the bottom right and top left quadrants of the autocorrelation functions for these dislocation types fluctuate between correlation and anticorrelation of varying strength. These fluctuations have wavelengths of tens of micrometers and switch between being dominated by anticorrelation or correlation approximately every 50–70 μm. The autocorrelation functions for the other dislocation types typically exhibit correlation over distances of approximately 10–40 μm but are generally uncorrelated over longer length scales.

3.4. Elastic Strain and Residual Stress Variations

For both samples analyzed here, maps of individual components of the (relative) elastic strain tensor contain sets of structures comparable to some of those evident in the distributions of lattice rotations and GND densities (Figures 10 and 11). In the $[011]_c$ sample, maps of the ε_{11}, ε_{22}, and ε_{12} components (i.e., the in-plane components) of the strain tensor reveal periodic bands aligned with the Set 2 GND structures. Variations in the magnitude of each component of the strain tensor between these bands are on the order of 10^{-3} (compared to 10^{-2} radians for the lattice rotations; Figure 5). Less common structures, aligned with the Set 1 GND structures, consist of variations of similar magnitude in the same components of the strain tensor. Relatively little structure is visible in maps of the ε_{13}, ε_{23}, and ε_{33} components of the strain tensor.

In the $[110]_c$ sample, most structure is again present in maps of the ε_{11}, ε_{22}, and ε_{12} components of the strain tensor. These maps contain prominent bands of varying magnitudes of elastic strain aligned with the Set 3 GND structures. The arrays of microcracks (Set 4) are associated with relatively local perturbations in the strain fields. The variations in each map of these components of the strain tensor are typically on the order of 10^{-3} (compared to 10^{-2} radians for the lattice rotations; Figure 6). Again, the out-of-plane ε_{i3} components of the strain tensor exhibit less pronounced structure.

The heterogeneous distributions of elastic strains evident in Figures 10 and 11 correspond to heterogeneous residual stresses, which remain in the sample even after removal of the external load (Figures 10 and 11). In the $[011]_c$ sample, structures evident as banded stress heterogeneities are present in the maps of the σ_{ac}, σ_{bc}, and σ_{cc}, components of the stress tensor. This notation of the components of the stress tensor refers to the stresses in the crystal reference frame. Thus, σ_{ac} describes stress acting in the [100] direction on the (001) plane and vice versa, due to the symmetries of both the stress tensor and crystal lattice. The magnitudes of these heterogeneities are on the order of 100 MPa. Notably, this is the same order of magnitude as the applied differential stress during deformation. The structure evident in the stress distributions is comparable to the structures in maps of the ε_{11}, ε_{22}, and ε_{12} components of the strain tensor and to Set 2 GND structures. Gradients extending across the whole map areas, for example, in the map of σ_{bb} in Figure 10, potentially result from slight errors in the position of the pattern center and therefore are not interpreted further. The map of σ_{aa} contains little structure as the [100] direction is approximately normal to the specimen surface, on which the normal stress is assumed relaxed.

Stress heterogeneities are also evident in the $[110]_c$ sample (Figure 11). Maps of the σ_{aa}, σ_{bb}, σ_{ab}, and σ_{ac} components of the stress tensor display bands of varying residual stress aligned with the structure seen in maps of the ε_{11}, ε_{22}, and ε_{12} components of the strain tensor and Set 3 GND structures (Figure 11). Prominent local perturbations in the fields of the σ_{aa}, σ_{bb}, and σ_{ab} components of the stress tensor are

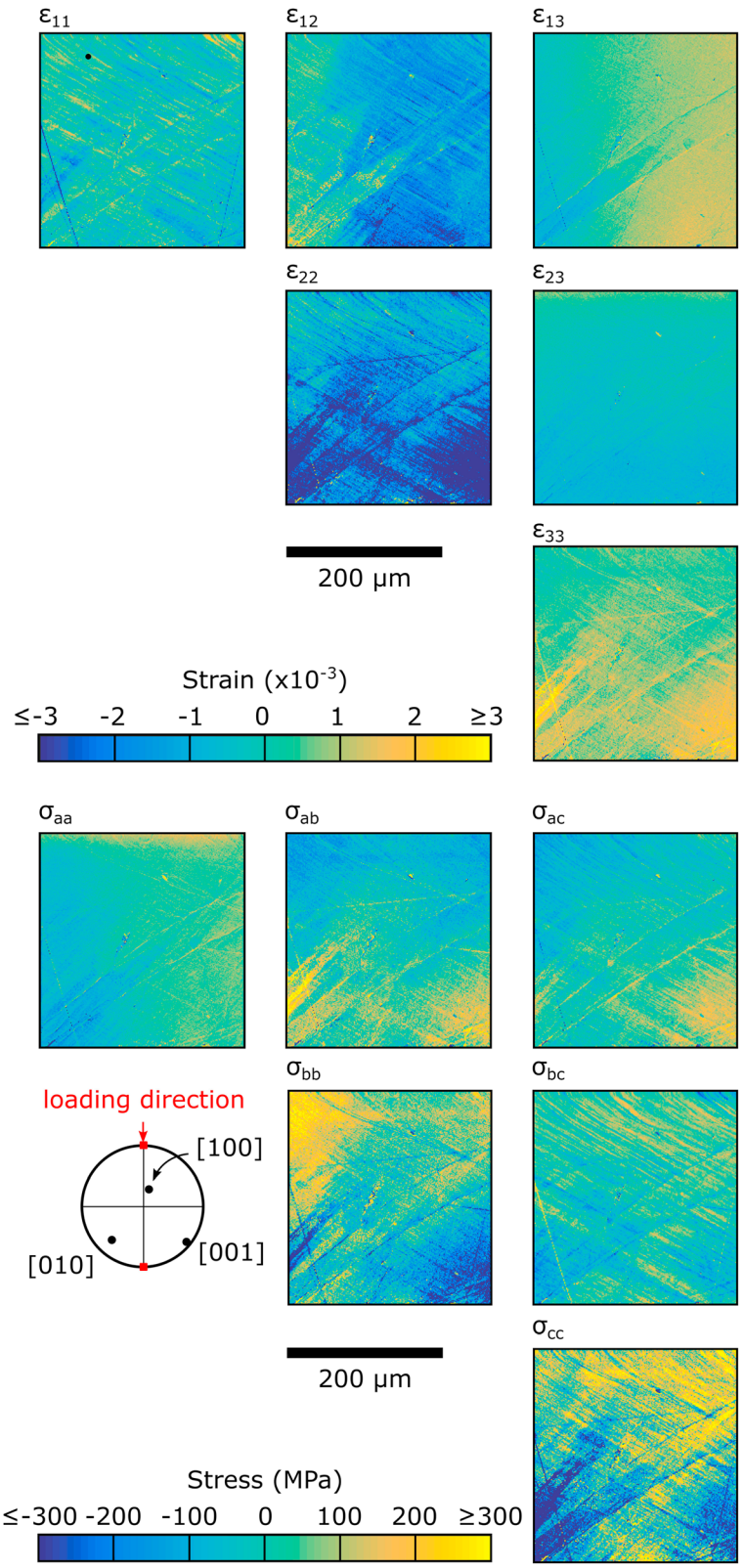

Figure 10. Elastic strains and residual stresses in the $[011]_c$ sample. Elastic strains are represented by one map for each component of the symmetric strain tensor (ε_{ij}), describing the strain state at each pixel relative to that of the reference point (black point in map of ε_{12}). The tensor ε_{ij} is in the reference frame of the EBSD map. Residual stresses are represented by one map for each component of the symmetric stress tensor (σ_{ij}) describing the stress state at each pixel relative to that of the reference point. The tensor σ_{ij} is in the crystal reference frame to illustrate variations in the residual stresses acting on each slip system.

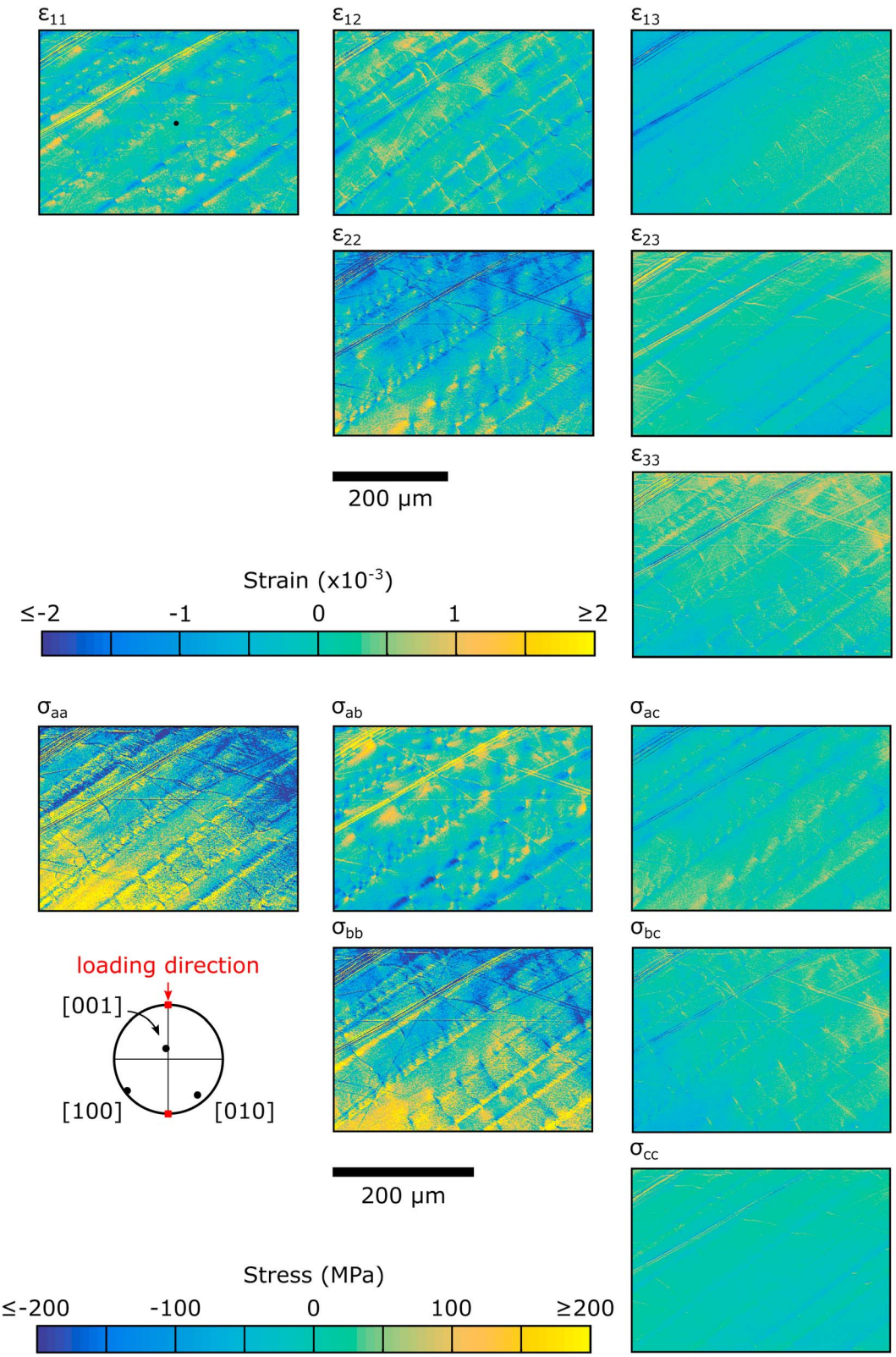

Figure 11. Elastic strains and residual stresses in the $[110]_c$ sample. Elastic strains are represented by one map for each component of the symmetric strain tensor (ε_{ij}) describing the strain state at each pixel relative to that of the reference point (black point in the map of ε_{12}). The tensor ε_{ij} is in the reference frame of the EBSD map. Residual stresses are represented by one map for each component of the symmetric stress tensor (σ_{ij}) describing the stress state at each pixel relative to that of the reference point. The tensor σ_{ij} is in the crystal reference frame to illustrate variations in the residual stresses acting on each slip system.

associated with the arrays of microcracks (Set 4). In the map of σ_{ab}, these perturbations form dipoles of positive and negative stresses at each of the crack tips. The magnitudes of stress heterogeneities, both between the bands and associated with the microcracks, are on the order of 100 MPa. The map of σ_{cc} contains little structure as the [001] direction is approximately normal to the specimen surface, on which the normal stress is assumed relaxed.

4. Discussion

4.1. Comparison to Published Flow Laws

The mechanical data presented in Figure 3 can be compared to previously published flow laws for olivine single crystals to gain insight into the operative deformation mechanisms. Bai et al. (1991) derived flow laws for single crystals of olivine from deformation experiments conducted at higher temperatures than the present study. Extrapolation of their flow law for $[110]_c$ oriented samples to a temperature of 1200°C closely predicts the strain rates of our $[110]_c$ sample (Figure 3). Therefore, we infer that this sample deformed by dislocation creep. In contrast, extrapolation of the flow law of Bai et al. (1991) for $[011]_c$ oriented samples to a temperature of 1000°C underestimates the strain rates of our $[011]_c$ sample by over 3 orders of magnitude (Figure 3). This difference implies the operation of an additional deformation mechanism, which was probably low-temperature plasticity. Therefore, in Figure 3, we compare the experimental data to the commonly used flow law of Evans and Goezte (1979) for low-temperature plasticity, and the recently published flow law of Idrissi et al. (2016). The flow laws for low-temperature plasticity are in better agreement with the experimental data for the $[011]_c$ sample than is the flow law of Bai et al. (1991), indicating a large contribution of low-temperature plasticity to the strain rate.

4.2. Comparison to Dislocation Structures in Previous Experiments on Single Crystals of Olivine

Dislocation microstructures in single crystals of olivine deformed in similar orientations to the samples in this study have been described in several previous works (Bai & Kohlstedt, 1992; Cooper et al., 2016; Durham et al., 1977; Hanson & Spetzler, 1994). In these studies, dislocations were imaged using decoration by oxidation (Kohlstedt et al., 1976). Therefore, the types of dislocations were inferred from the crystallographic orientations of dislocation lines, the loading directions, and shape changes of the samples. The densities of decorated dislocations in our samples (Figure 4) are broadly consistent with the relationship between dislocation density and differential stress found by Bai and Kohlstedt (1992) extrapolated to higher differential stresses. However, dislocation densities obtained from decoration are not directly comparable to GND densities obtained from HR-EBSD as the fraction of the dislocation population that contributes to measured lattice curvature (i.e., appears as GNDs) typically varies with mapping step size and depends on the precise arrangement of dislocations (Jiang et al., 2013b; Wallis et al., 2016). We note also that it is not possible to predict which dislocations were free to glide during deformation based solely on whether they appear as GNDs or SSDs as their mobility depends on other factors in addition to their spatial relationship to other dislocations.

For samples loaded in the $[011]_c$ orientation, the (010)[001] slip system has the greatest resolved shear stress (Durham et al., 1977). However, only very slight misorientation from this ideal geometry is required to activate dislocations with [100] Burgers vectors (Bai & Kohlstedt, 1992; Cooper et al., 2016; Darot & Gueguen, 1981). In our nominally $[011]_c$ sample, the [100] axis is oriented at 66° to the loading direction, so activation of dislocations with [100] Burgers vectors is expected in addition to those with [001] Burgers vectors. Previous studies noted that screw dislocations with both [001] and [100] Burgers vectors are ubiquitous in samples deformed in the $[011]_c$ orientation, and these are often arranged into twist boundaries (Bai & Kohlstedt, 1992; Cooper et al., 2016; Durham et al., 1977). Structures with significant quantities of [001] and [100] screw dislocations are also present in our $[011]_c$ sample, particularly in Set 1 (Figure 5). These dislocation types are spatially correlated (Figure 7), suggesting that these bands may also have a significant component of twist character. However, previous studies have primarily suggested twist boundaries to be parallel to (010), which is expected from a net of [001] and [100] screw dislocations (Bai & Kohlstedt, 1992; Cooper et al., 2016; Durham et al., 1977). The Set 1 structures in our sample appear to be at a high angle to (010). However, it is still possible that the boundary is faceted at small length scales with local segments parallel to (010), a feature referred to as "zig-zag lines" by Bai and Kohlstedt (1992) in their Figure 8d.

Set 2 structures in the $[011]_c$ sample contain (010)[001] edge dislocations (blue arrows in Figures 4 and 5). Therefore, these structures are consistent with the (010)[001] slip system being activated in the $[011]_c$ loading orientation (Cooper et al., 2016; Durham et al., 1977). As the [001] Burgers vector is parallel to the trace of these structures (Figures 1 and 5), Wallis et al. (2016) interpreted them to be slip bands of (010)[001] edge dislocations (e.g., Figure 2). These bands resemble the closely spaced, low-angle structures observed in crystals deformed in the same orientation by Durham et al. (1977). Note that the orientation and spacing of these structures are similar to those interpreted by Bai and Kohlstedt (1992) (their Figure 7b) and Cooper et al. (2016) (their Figure 8a) to also be (010) twist walls. We emphasize that the zig-zag lines discussed above and observed by Durham et al. (1977) and Bai and Kohlstedt (1992) have high dislocation densities and are convincingly interpreted as twist walls (especially considering the transmission electron microscopy (TEM) observations of Durham et al., 1977). However, the detailed views of bands parallel to (010) presented by Bai and Kohlstedt (1992) and Cooper et al. (2016) have much lower dislocation densities without any faceting and may alternatively be interpreted, in a manner consistent with our data, to be slip bands of (010)[001] edge dislocations.

For single crystals of olivine loaded in the $[110]_c$ orientation, the (010)[100] slip system has the greatest resolved shear stress, and previous investigations of samples deformed in this orientation consistently report microstructures that indicate the activity of this slip system (Bai & Kohlstedt, 1992; Durham et al., 1977; Hanson & Spetzler, 1994). These microstructures include edge dislocations and loops with [100] Burgers vectors arranged along (010) slip planes or arranged in subgrain boundaries parallel to the (100) plane (Bai & Kohlstedt, 1992; Durham et al., 1977; Hanson & Spetzler, 1994). Maps of GND densities in our $[110]_c$ sample reveal little structure composed of (010)[100] edge dislocations (except apparent GND density resulting from microcracks) (Figure 6). In this sample, screw dislocations with [100] Burgers vectors are present in Set 3, although these structures are also primarily composed of (001)[100] edge dislocations (Figure 6). These observations suggest that dislocations of the (010)[100] slip system, if present, may be arranged such that they do not contribute significant macroscopic curvature across the 1 μm length scale of the EBSD step size; i.e., they are primarily statistically stored dislocations (SSDs). Similarly, tilt walls composed of (010)[100] edge dislocations commonly observed in previous studies (e.g., Bai & Kohlstedt, 1992; Durham et al., 1977) are not evident in our $[110]_c$ sample (Figure 6). Durham et al. (1977) found that the dislocation structure, including (100) tilt walls, was well established by approximately 4% strain. However, in the experiments of Karato et al. (1980) polygonized substructure did not develop until strains of 20–40% had been attained. Therefore, it remains possible that the strain of 14.67% experienced by our $[110]_c$ sample was insufficient for subgrain boundaries to fully develop. In contrast, GNDs of (001)[100] edge character are present in relatively high densities and arranged in prominent bands of Set 3. These structures are similar to slip bands in that the Burgers vector of these dislocations is parallel to the trace of the bands. However, discrete slip bands are not evident in the distribution of decorated dislocations (Figure 4), and instead, the Set 3 structures consist of broader swathes dominated by dislocations of particular types and sense of Burgers vector.

Overall, the dislocation types and distributions that we observe in both samples are broadly consistent with those described in previous studies of single crystals of olivine, within the limitations of the various observational techniques (Bai & Kohlstedt, 1992; Cooper et al., 2016; Durham et al., 1977; Hanson & Spetzler, 1994; Wallis et al., 2016). However, our results systematically distinguish different types of GNDs and map their distributions over 10^{-4} m length scales. These quantitative data sets allow us to characterize the distributions of dislocations in new detail and interpret the processes that give rise to both the distributions of each dislocation type and relationships between dislocation types.

4.3. Interpretation of Dislocation Interactions

A notable feature of the GND density distributions mapped in this study is that each set of GND structures consists of multiple dislocation types (Figures 5–7). Systematic mapping of the spatial relationships between dislocation types across representative areas would not be possible using decoration or TEM, and their identification raises a new question as to how such relationships arise.

One possibility is that each set of GND structures results from discrete boundaries with complex lattice-scale structure composed of multiple dislocation types. This is potentially true for the correlation between [100] and [001] screw dislocations in the $[011]_c$ sample (Figures 5 and 7), which is expected based on previous studies, and potentially represents boundaries with dominantly twist character (Bai & Kohlstedt, 1992; Cooper

et al., 2016; Durham et al., 1977). The strong correlation between these dislocation types and (001)[100] edge dislocations (Figures 5 and 7) may result from the presence of boundaries with mixed character, rather than pure twist (Wallis et al., 2016). However, the other correlations between dislocation types observed in this study (Figures 5–7) have not been reported previously.

A second and potentially more general explanation is that such spatial correlations may arise from resistance to glide of one dislocation type by short-range interactions with another dislocation type. This hypothesis is supported by the observation that dislocation types within each pair that exhibits a notably elevated correlation coefficient are capable of mutually exerting glide forces that may influence their motion (Figure 7). Impedance of dislocations gliding in their slip planes is evidenced by clusters of dislocations in slip bands (Set 2 structures) in the $[011]_c$ sample (Figure 4). Previous numerical and TEM investigations of such interactions in olivine deformed at temperatures of 800–900°C inferred that collinear interactions, between dislocations with [001] Burgers vectors on different glide planes, are the dominant short-range interaction (Durinck et al., 2007; Mussi et al., 2015). However, for our samples deformed at higher temperatures of 1000°C and 1200°C, correlation coefficients between different dislocation types with [001] Burgers vectors are less than 0.4 (Figure 7). These weak correlations suggest that at these temperatures collinear interactions between dislocations with [001] Burgers vectors are less important for inhibiting glide than other types of interaction. Most of the strong correlations between dislocation types, with coefficients greater then 0.5, in both samples are between dislocations with perpendicular Burgers vectors (Figures 5–7). These correlations indicate that noncollinear interactions may pose stronger impediments to dislocation glide than collinear interactions at these temperatures. In the $[011]_c$ sample, (001)[100] edge and [100] screw dislocations have a correlation coefficient of 0.88 (Figure 7). This strong correlation could arise from the presence of dislocation loops with [100] Burgers vectors or from complex boundary structures. In summary, noncollinear short-range interactions between dislocations appear to have played an important role in the development of the sets of dislocation structures.

Another characteristic of the GND density distributions in both samples is that the sets of structures typically consist of alternating bands of dislocations of opposite sign (Figures 5 and 6). In other words, the dislocations in adjacent bands generally have net Burgers vectors of opposite sense, resulting in alternating senses of lattice curvature. This structure is evident also in the autocorrelation functions of each map of GND density, where it manifests as periodic correlation-anticorrelation (Figures 8 and 9). We note that the opposite signs of the GNDs inhibit net macroscopic curvature of the sample, consistent with the imposed axial shortening. However, the segregation of GNDs with opposite sign into separate bands, and the length scales over which this occurs, is particularly interesting. The apparent length scales over which particular types of GNDs are correlated and/or anticorrelated typically range from a few micrometers up to tens of micrometers (Figure 9). Due to the sectioning effect, the apparent spacing of bands of elevated GND density in our maps provides an upper bound on their true spacing in 3-D. Slip bands, with dislocations in alternate bands having opposite Burgers vectors, have long been recognized in the materials sciences and are termed "dipolar mats" (Fourie et al., 1982; Hansen & Kuhlmann-Wilsdorf, 1986; Kuhlmann-Wilsdorf & Comins, 1983). Dislocations in dipolar mats may be evenly spaced or may be heterogeneously spaced as a result of local pileups (Fourie et al., 1982; Hansen & Kuhlmann-Wilsdorf, 1986). Such structures can be clearly recognized in the $[011]_c$ sample (Figures 4 and 5), whereas the $[110]_c$ sample contains bands of dislocations of opposite sign, but their slip band arrangement appears to have been disrupted by enhanced climb due the higher deformation temperature (Figures 4 and 6). Bands of dislocations of opposite sign, including dipolar mats, are low-energy arrangements of dislocations because internal stresses arising from each band are reduced over length scales greater than the spacing of each pair of bands (Hansen & Kuhlmann-Wilsdorf, 1986). As forces are always directed so as to decrease free energy, dislocations are driven to segregate into bands with opposing Burgers vectors, senses of lattice curvature, and associated stress fields (Kuhlmann-Wilsdorf & Comins, 1983). Moreover, internal stresses between the bands of a primary dislocation type may enhance activation of secondary slip systems, which further lower the free energy (Kuhlmann-Wilsdorf & Comins, 1983). The internal stress heterogeneities mapped in our samples (Figures 10 and 11) may therefore have contributed to the diversity of dislocation types present (Figures 5 and 6). The characteristic band spacings that arise are likely controlled by the efficiency with which dislocations with opposite Burgers vectors can annihilate by climb. This inference is consistent with the larger band spacings in the sample deformed at 1200°C than in the sample deformed at 1000°C (Figures 5, 6, and 9).

The maps of heterogeneity in residual stress within these single crystals of olivine (Figures 10 and 11) provide a test for the hypothesis that long-range internal stresses arise from accumulations of GNDs. Heterogeneities in residual stress, typically on the order of 100 MPa, are present in both samples (Figures 10 and 11). These heterogeneities are of the same order of magnitude as the applied differential stress during deformation. Moreover, the heterogeneities in residual stress (Figures 10 and 11) reveal structure similar to that evident in the distributions of GND densities (Figures 5 and 6), despite being derived from independent aspects of the data (i.e., the strains and rotations, respectively). In particular, in the $[011]_c$ sample, the σ_{bc} component of stress (Figure 10) exhibits structure similar to that of the slip bands of (010)[001] edge dislocations (Figure 5). Importantly, this component of the stress tensor induces a glide force on (010)[001] dislocations. These observations are consistent with the dislocations within the slip bands exerting significant back-stresses during deformation, which are expressed as residual stress after removal of the external load. Such back-stresses provide a plausible explanation for the irregular spacing of dislocations within slip bands in the $[011]_c$ sample (Figure 4). In the $[110]_c$ sample, stress heterogeneities (Figure 11) are also spatially associated with the bands of high dislocation density (Figure 6). More generally, although it remains difficult to quantitatively interpret the internal stress distribution *during* deformation, the similarities in the distributions of residual stress and GND density constitute new and compelling evidence for the presence of long-range internal stresses and their role in dislocation processes in olivine. Support for this interpretation comes from dislocation dynamics simulations that consider the stress state arising from the combination of externally applied stress and the intrinsic stress field around dislocations (Boioli, Tommasi, et al., 2015). These simulations predict stress heterogeneities on the order of 100 MPa, varying over micrometer length scales (Boioli, Tommasi, et al., 2015), very similar to the residual stress distributions in our samples (Figures 10 and 11). Additional verification for the presence of such stress heterogeneities during deformation is provided by analysis of the microcracks in the $[110]_c$ sample. The presence of cracks on the order of 20 μm long and our measurements of tensile stresses of 200 MPa normal to the cracks imply a critical stress intensity for crack propagation (K_{1c}) of approximately 1 MPa $m^{0.5}$. This value is of a similar order as theoretical and experimental estimates of intragranular K_{1c} in olivine (e.g., Tromans & Meech, 2002).

To summarize, the banded GND density distributions, often with Burgers vectors within the planes of the structures, can be expected to form as a kinematic response to the applied loading. Slip bands have been observed previously in olivine single crystals but have not been studied in detail (Bai & Kohlstedt, 1992). However, their identification and characterization is significantly aided by HR-EBSD (Wallis et al., 2016; this study). The correlations of dislocation types in the principle structures (Figures 5–7) likely arise from short-range interactions between the different dislocation types. These short-range interactions resulted in accumulations of dislocations along slip bands in the $[011]_c$ sample and heterogeneous GND densities in both samples (Figures 5 and 6). The spatial correlations between different dislocation types in our samples (Figure 7) deformed at 1000°C and 1200°C indicate a significant role for noncollinear interactions in the development of substructure. This finding contrasts with previous work which found evidence for primarily collinear interactions in samples deformed at temperatures below 900°C (Mussi et al., 2015) and therefore raises the possibility that the dominant type of short-range interaction may vary with temperature. Lattice distortion around regions of high dislocation density generated internal stress heterogeneities of the same order of magnitude as the applied stress during deformation (Figures 10 and 11). These internal stresses would have significantly modified the effective stress state (Evans et al., 1985; Mughrabi, 1983; Mughrabi et al., 1986; Viatkina et al., 2007), impacting the development and organization of the dislocation substructure through long-range dislocation interactions (Montagnat et al., 2006).

4.4. Implications for Mantle Rheology

Extrapolation of laboratory-derived flow laws to describe deformation under the environmental and mechanical conditions typical of the upper mantle requires that the same microphysical processes control the rheological behavior in both settings (Bai & Kohlstedt, 1992; Hirth & Kohlstedt, 2003). For deformation occurring by motion of dislocations, ensuring that this condition is met necessarily entails identifying impediments to rates of dislocation glide and the mechanisms by which they are overcome. Experiments designed specifically to investigate dislocation interactions in single crystals of olivine at 1550–1600°C found no evidence that interactions between dislocation types modified either the microstructures or mechanical properties compared to those generated by activation of single slip systems in isolation (Durham et al., 1985).

However, TEM observations and modeling suggest that interactions between dislocations may modify glide behavior at temperatures of 800–1000°C (Boioli, Carrez, et al., 2015; Boioli, Tommasi, et al., 2015; Durinck et al., 2007; Mussi et al., 2015). Our analysis of olivine deformed at 1000°C and 1200°C strongly suggests that interactions between different dislocation types hindered dislocation glide, impacted the development of substructure, and thereby presumably exerted an influence on mechanical properties. In the $[011]_c$ sample, deformed with a large contribution of low-temperature plasticity at 1000°C, irregular dislocation spacings along slip bands (Figure 4) indicate that dislocation interactions imposed additional resistance to glide on top of that arising from lattice friction. Correlations between dislocation types indicate that dislocation interactions also hindered glide in the $[110]_c$ sample deformed by dislocation creep at 1200°C (Figure 7), but the lack of discrete slip bands (Figure 4) suggests that such obstacles were overcome by climb. The combination of these observations/studies suggests that the significance of dislocation interactions varies with temperature. Therefore, this study raises three questions which must be answered in order to determine the roles and impacts of dislocation interactions during deformation by low-temperature plasticity and dislocation creep. First, how do the temperature dependencies of glide resistance from lattice friction, glide resistance from dislocation interactions, and dislocation climb/cross-slip trade-off? Second, to what extent do dislocations overcome the glide resistance imposed by interactions with other dislocations by nonconservative climb/cross-slip versus conservative bowing out or "punching through"? Lastly, what evidence for dislocation interactions is preserved in exhumed mantle rocks? Answers to the first two questions will improve the mechanistic basis for models of mantle flow, and an answer to the third will help confirm the reliability of extrapolating laboratory-derived models to real Earth conditions.

5. Conclusions

Single crystals of olivine deformed in triaxial compression under varied deformation conditions exhibit periodic variation in densities and signs of GNDs. Several wavelengths of these substructures are expressed in the distributions of various types of GND and span length scales of micrometers to tens of micrometers. Spatial correlations between different dislocation types are evident in both samples. Variations in elastic strain and residual stress on the orders 10^{-3} and 100 MPa, respectively, are spatially coincident with areas of high GND density and exhibit similar structure and length scales in their distributions. The results indicate that dislocation glide is hindered by short-range interactions that may transition from being primarily collinear to noncollinear with increasing temperature, leading to local accumulations of high dislocation densities. These accumulations of dislocations generate elastic strain gradients and variations in residual stress that likely exert long-range influences on dislocation motion. Evidence for organization spanning length scales of micrometers to tens of micrometers is preserved in the spatial distributions of GNDs and is likely influenced by long-range dislocation interactions. Both short-range interactions and the substructure and stress fields that develop over longer length scales potentially impact dislocation glide. Determining the dislocation interactions that occur over a wide range of both natural and experimental conditions, and the mechanisms by which dislocations overcome any impediments to glide that result, is therefore key to understanding the controls on rheological properties of mantle rocks undergoing tectonic deformation.

Acknowledgments
We thank David Kohlstedt and Steven Schneider for providing samples for this study and Andrew Turner for helpful discussions. We thank Greg Hirth and David Kohlstedt for their constructive reviews of the manuscript. D. Wallis, L.N. Hansen, and A.J. Wilkinson acknowledge support from the Natural Environment Research Council grant NE/M000966/1. T.B. Britton acknowledges support for his research fellowship from the Royal Academy of Engineering. Research data supporting this paper can be found on the Oxford Research Archive (http://www.ora.ox.ac.uk/).

References

Abramson, E. H., Brown, J. M., Slutsky, L. J., & Zaug, J. (1997). The elastic constants of San Carlos olivine to 17 GPa. *Journal of Geophysical Research*, *102*, 12,253–12,263. https://doi.org/10.1029/97JB00682

Bai, Q., & Kohlstedt, D. L. (1992). High-temperature creep of olivine single crystals, 2. Dislocation structures. *Tectonophysics*, *206*, 1–29. https://doi.org/10.1016/0040-1951(92)90365-D

Bai, Q., Mackwell, S. J., & Kohlstedt, D. L. (1991). High-temperature creep of olivine single crystals 1. Mechanical results for buffered samples. *Journal of Geophysical Research*, *96*, 2441–2463. https://doi.org/10.1029/90JB01723

Boioli, F., Carrez, P., Cordier, P., Devincre, B., & Marquille, M. (2015). Modelling the creep properties of olivine by 2.5-dimensional dislocation dynamics simulations. *Physical Review B*, *92*, 014115. https://doi.org/10.1103/PhysRevB.92.014115

Boioli, F., Tommasi, A., Cordier, P., Demouchy, S., & Mussi, A. (2015). Low steady-state stresses in the cold lithospheric mantle inferred from dislocation dynamics models of dislocation creep in olivine. *Earth and Planetary Science Letters*, *432*, 232–242. https://doi.org/10.1016/j.epsl.2015.10.012

Britton, T. B., & Wilkinson, A. J. (2011). Measurement of residual elastic strain and lattice rotations with high resolution electron backscatter diffraction. *Ultramicroscopy*, *111*, 1395–1404. https://doi.org/10.1016/j.ultramic.2011.05.007

Britton, T. B., & Wilkinson, A. J. (2012a). High resolution electron backscatter diffraction measurements of elastic strain variations in the presence of larger lattice rotations. *Ultramicroscopy*, *114*, 82–95. https://doi.org/10.1016/j.ultramic.2012.01.004

Britton, T. B., & Wilkinson, A. J. (2012b). Stress fields and geometrically necessary dislocation density distributions near the head of a blocked slip band. *Acta Materialia*, *60*, 5773–5782. https://doi.org/10.1016/j.actamat.2012.07.004

Cooper, R. F., Stone, D. S., & Plookphol, T. (2016). Load relaxation of olivine single crystals. *Journal of Geophysical Research: Solid Earth*, *121*, 7193–7210. https://doi.org/10.1002/2016JB013425

Darot, M., & Gueguen, Y. (1981). High-temperature creep of forsterite single crystals. *Journal of Geophysical Research*, *86*, 6219–6234. https://doi.org/10.1029/JB086iB07p06219

Demouchy, S., Schneider, S. E., Mackwell, S. J., Zimmerman, M. E., & Kohlstedt, D. L. (2009). Experimental deformation of olivine single crystals at lithospheric temperatures. *Geophysical Research Letters*, *36*, L04304, https://doi.org/10.1029/2008GL036611

Demouchy, S., Tommasi, A., Ballaran, T. B., & Cordier, P. (2013). Low strength of Earth's uppermost mantle inferred from tri-axial deformation experiments on dry olivine crystals. *Physics of the Earth and Planetary Interiors*, *220*, 37–49. https://doi.org/10.1016/j.pepi.2013.04.008

Durham, W. B., & Goetze, C. (1977). Plastic flow of oriented single crystals of olivine: 1. Mechanical data. *Journal of Geophysical Research*, *82*, 5737–5753. https://doi.org/10.1029/JB082i036p05737

Durham, W. B., Goetze, C., & Blake, B. (1977). Plastic flow of oriented single crystals of olivine: 2. Observations and interpretations of the dislocation structures. *Journal of Geophysical Research*, *82*, 5755–5770. https://doi.org/10.1029/JB082i036p05755

Durham, W. B., Ricoult, D. L., & Kohlstedt, D. L. (1985). Interaction of slip systems in olivine. In R. N. Schock (Ed.), *Point Defects in Minerals* (pp. 185–193). Washington, DC: American Geophysical Union. https://doi.org/10.1029/GM031p0185

Durinck, J., Devincre, B., Kubin, L., & Cordier, P. (2007). Modeling the plastic deformation of olivine by dislocation dynamics simulations. *American Mineralogist*, *92*, 1346–1357. https://doi.org/10.2138/am.2007.2512

Evans, B., & Goezte, C. (1979). The temperature variation of hardness of olivine and its implications for polycrystalline yield stress. *Journal of Geophysical Research*, *84*, 5505–5524. https://doi.org/10.1029/JB084iB10p05505

Evans, R. W., Roach, W. J. F., & Wilshire, B. (1985). Creep of aluminium following stress reductions. *Scripta Metallurgica*, *19*, 999–1003. https://doi.org/10.1016/0036-9748(85)90299-6

Fourie, J. T., Jackson, P. J., Kuhlmann-Wilsdorf, D., Rigney, D. A., van der Merwe, J. H., & Wilsdorf, H. G. F. (1982). Nomenclature for dislocation arrays. *Scripta Metallurgica*, *16*, 157–160. https://doi.org/10.1016/0036-9748(82)90376-3

Girard, J., Chen, J., Raterron, P., & Holyoke, C. W. III (2013). Hydrolytic weakening of olivine at mantle pressure: Evidence of [100](010) slip system softening from single-crystal deformation experiments. *Physics of the Earth and Planetary Interiors*, *216*, 12–20. https://doi.org/10.1016/j.pepi.2012.10.009

Hansen, L. N., Zimmerman, M. E., & Kohlstedt, D. L. (2012). The influence of microstructure on deformation of olivine in the grain-boundary sliding regime. *Journal of Geophysical Research*, *117*, B09201. https://doi.org/10.1029/2012JB009305

Hansen, N., & Kuhlmann-Wilsdorf, D. (1986). Low energy dislocation structures due to unidirectional deformation at low temperatures. *Materials Science and Engineering*, *81*, 141–161. https://doi.org/10.1016/0025-5416(86)90258-2

Hanson, D. R., & Spetzler, H. A. (1994). Transient creep in natural and synthetic, iron-bearing olivine single crystals: Mechanical results and dislocation microstructures. *Tectonophysics*, *235*, 293–315. https://doi.org/10.1016/0040-1951(94)90191-0

Hirth, G., & Kohlstedt, D. (2003). Rheology of the mantle wedge: A view from the experimentalists. In J. Eiler (Ed.), *Inside the Subduction Factory* (pp. 83–105). Washington, DC: American Geophysical Union. https://doi.org/10.1029/138GM06

Hirth, G., & Kohlstedt, D. (2015). The stress dependence of olivine creep rate: Implications for extrapolation of lab data and interpretation of recrystallized grain size. *Earth and Planetary Science Letters*, *418*, 20–26. https://doi.org/10.1016/j.epsl.2015.02.013

Idrissi, H., Bollinger, C., Boioli, F., Schryvers, D., & Cordier, P. (2016). Low-temperature plasticity of olivine revisited with in situ TEM nanomechanical testing. *Science Advances*, *2*, e1501671. https://doi.org/10.1126/sciadv.1501671

Jiang, J., Britton, T. B., & Wilkinson, A. J. (2013a). Mapping type III intragranular residual stress distributions in deformed copper polycrystals. *Acta Materialia*, *61*, 5895–5904. https://doi.org/10.1016/j.actamat.2013.06.038

Jiang, J., Britton, T. B., & Wilkinson, A. J. (2013b). Measurement of geometrically necessary dislocation density with high resolution electron backscatter diffraction: Effects of detector binning and step size. *Ultramicroscopy*, *125*, 1–9. https://doi.org/10.1016/j.ultramic.2012.11.003

Jiang, J., Zhang, T., Dunne, F. P. E., & Britton, T. B. (2015). Deformation compatibility in a single crystalline Ni superalloy. *Proceedings of the Royal Society A*, *472*, 20150690. https://doi.org/10.1098/rspa.2015.0690

Karato, S.-I., & Wu, P. (1993). Rheology of the Upper Mantle: A Synthesis. *Science*, *260*, 771–778. https://doi.org/10.1126/science.260.5109.771

Karato, S.-I., Toriumi, M., & Fujii, T. (1980). Dynamic recrystallisation of olivine single crystals during high-temperature creep. *Geophysical Research Letters*, *7*, 649–652. https//doi.org/10.1029/GL007i009p00649

Kohlstedt, D. L., & Goetze, C. (1974). Low-stress high-temperature creep in olivine single crystals. *Journal of Geophysical Research*, *79*, 2045–2051. https://doi.org/10.1029/JB079i014p02045

Kohlstedt, D. L., & Hansen, L. N. (2015). Constitutive equations, rheological behaviour, and viscosity of rocks. In G. Schubert (Ed.), *Treatise on Geophysics* (Vol. 2, pp. 441–472). Oxford: Elsevier.

Kohlstedt, D. L., Goetze, C., Durham, W. B., & Vander Sande, J. (1976). New technique for decorating dislocations in olivine. *Science*, *191*, 1045–1046. https://doi.org/10.1126/science.191.4231.1045

Kuhlmann-Wilsdorf, D., & Comins, N. R. (1983). Dislocation cell formation and work hardening in the unidirectional glide of F.C.C. metals I: Basic theoretical analysis of cell walls parallel to the primary glide plane in early stage II. *Materials Science and Engineering*, *60*, 7–24. https://doi.org/10.1016/0025-5416(83)90073-3

Mackwell, S. J., Kohlstedt, D. L., & Paterson, M. S. (1985). The role of water in the deformation of olivine single crystals. *Journal of Geophysical Research*, *90*, 11,319–11,333. https://doi.org/10.1029/JB090iB13p11319

Mikami, Y., Oda, K., Kamaya, M., & Mochizuki, M. (2015). Effect of reference point selection on microscopic stress measurement using EBSD. *Materials Science and Engineering A*, *647*, 256–264. https://doi.org/10.1016/j.msea.2015.09.004

Montagnat, M., Weiss, J., Chevy, J., Duval, P., Brunjail, H., Bastie, P., & Gil Sevillano, J. (2006). The heterogeneous nature of slip in ice single crystals deformed under torsion. *Philosophical Magazine*, *86*, 4259–4280. https://doi.org/10.1080/14786430500452602

Mughrabi, H. (1983). Dislocation wall and cell structures and long-range internal stresses in deformed metal crystals. *Acta Metallurgica*, *31*, 1367–1379. https://doi.org/10.1016/0001-6160(83)90007-X

Mughrabi, H., Ungár, T., Kienle, W., & Wilkens, M. (1986). Long-range internal stresses and asymmetric X-ray line-broadening in tensile-deformed [001]-oriented copper single crystals. *Philosophical Magazine*, *53*, 793–813. https://doi.org/10.1080/01418618608245293

Mussi, A., Cordier, P., & Demouchy, S. (2015). Characterization of dislocation interactions in olivine using electron tomography. *Philosophical Magazine*, *95*, 335–345. https://doi.org/10.1080/14786435.2014.1000996

Nye, J. F. (1953). Some geometrical relations in dislocated crystals. *Acta Metallurgica*, *1*, 153–162. https://doi.org/10.1016/0001-6160(53)90054-6

Paterson, M. S. (1976). Some current aspects of experimental rock deformation. *Philosophical Transactions of the Royal Society A*, *283*, 163–172. https://doi.org/10.1098/rsta.1976.0076

Paterson, M. S. (1990). Rock deformation experimentation. In A. G. Duba, et al. (Eds.), *The Brittle Ductile Transition in Rocks: The Heard Volume*, *Geophysical Monograph Series* (pp. 187–194). Washington, DC: American Geophysical Union. https://doi.org/10.1029/GM056p0187

Peach, M., & Koehler, J. S. (1950). The forces exerted on dislocations and the stress fields produced by them. *Physical Review*, *80*, 436–439. https://doi.org/10.1103/PhysRev.80.436

Ruggles, T. J., Rampton, T. M., Khosravani, A., & Fullwood, D. T. (2016). The effect of length scale on the determination of geometrically necessary dislocations via EBSD continuum dislocation microscopy. *Ultramicroscopy*, *164*, 1–10. https://doi.org/10.1016/j.ultramic.2016.03.003

Schneider, S. E. (2008). Deformation of olivine single crystals at intermediate temperatures: Application to deformation of the lithosphere. MSc. thesis, University of Minnesota.

Tromans, D., & Meech, J. A. (2002). Fracture toughness and surface energies of minerals: Theoretical estimates for oxides, sulphides, silicates and halides. *Minerals Engineering*, *15*, 1027–1041. https://doi.org/10.1016/S0892-6875(02)00213-3

Turcotte, D. L., & Oxburgh, E. R. (1972). Mantle convection and the new global tectonics. *Annual Review of Fluid Mechanics*, *4*, 33–66. https://doi.org/10.1146/annurev.fl.04.010172.000341

Viatkina, E. M., Brekelmans, W. A. M., & Geers, M. G. D. (2007). Modelling of the internal stress in dislocation cell structures. *European Journal of Mechanics - A/Solids*, *26*, 982–998. https://doi.org/10.1016/j.euromechsol.2007.05.001

Wallis, D., Hansen, L. N., Britton, T. B., & Wilkinson, A. J. (2016). Geometrically necessary dislocation densities in olivine obtained using high-angular resolution electron backscatter diffraction. *Ultramicroscopy*, *168*, 34–45. https://doi.org/10.1016/j.ultramic.2016.06.002

Weertman, J. (1970). The creep strength of the Earth's mantle. *Reviews of Geophysics and Space Physics*, *8*, 145–168. https://doi.org/10.1029/RG008i001p00145

Wilkinson, A. J., & Randman, D. (2010). Determination of elastic strain fields and geometrically necessary dislocation distributions near nanoindents using electron back scatter diffraction. *Philosophical Magazine*, *90*, 1159–1177. https://doi.org/10.1080/14786430903304145

Wilkinson, A. J., Meaden, G., & Dingley, D. J. (2006). High-resolution elastic strain measurement from electron backscatter diffraction patterns: New levels of sensitivity. *Ultramicroscopy*, *106*, 307–313. https://doi.org/10.1016/j.ultramic.2005.10.001